Decadal changes of surface elevation over permafrost area estimated using reflected GPS signals

Lin Liu[1], Kristine M. Larson[2]

[1] Earth System Science Programme, Faculty of Science, The Chinese University of Hong Kong, Hong Kong, China.
[2] Department of Aerospace Engineering Sciences, University of Colorado, Boulder, CO, 80309, USA
Correspondence to: Lin Liu (liulin@cuhk.edu.hk)

Abstract. Conventional benchmark-based surveys and Global Positioning System (GPS) have been used to measure surface elevation changes over permafrost areas, usually once or a few times a year. Here we introduce a new method that uses reflected GPS signals to measure temporal changes of ground surface elevation due to dynamics of the active layer and near-surface permafrost. Applying the GPS interferometric reflectometry technique to the signal-to-noise-ratio data collected by a continuous GPS receiver mounted deep in permafrost in Barrow, Alaska, we can retrieve the vertical distance between the antenna and surface reflector under the antenna. Using this unique kind of observables, we obtain daily changes of surface elevation during July and August from 2004 to 2015. Our results show distinct temporal variations at three timescales: regular thaw settlement within each summer, strong inter-annual variability that is characterized by a sub-decadal subsidence trend followed by a brief uplift trend, and a secular subsidence trend of 0.26±0.02 cm/year during 2004 and 2015. This method provides a new way to fully utilize data from continuous GPS sites in cold regions for studying dynamics of the frozen ground consistently and sustainably over a long time.

1 Introduction

Over permafrost terrains the ground surface undergoes seasonal vertical displacements associated with the annual freeze/thaw cycle. Superimposed on the seasonal cycle, inter-annual and long-term changes of ground surface elevation may occur due to permafrost degradation/aggradation and subsurface water migration. Measuring and monitoring surface elevation changes at various timescales are critical to improving our understanding of the dynamics of the integrated system of permafrost and the active layer (i.e., the seasonally freezing/thawing layer on top of permafrost), to studying the impacts of permafrost changes on hydro-ecological systems, and to assessing the risk of permafrost changes to infrastructure such as buildings and roads.

Measurements of surface elevation changes over permafrost areas have been largely based on conventional benchmark-based surveys. The classical method is to use vertical tubes or pipes anchored deep in permafrost as datum benchmarks of the ground surface for repeat leveling surveys (e.g., Mackay and Burn, 2002). J. R. Mackay also developed a few instruments such as the heavemeter (also called heave tube), magnet probe, and access tube, specifically for measuring frost heave

(Mackay 1982; Mackay 1983; Mackay and Leslie, 1987). Using linear variable differential transformers, Harris et al. (2007) designed an instrument for monitoring solifluction movement, including surface elevation changes, in Svalbard.

Advancing from conventional to space geodetic methods, Little et al. (2003) carried out one of the first Global Positioning System (GPS) campaign surveys on tundra surface over permafrost areas. Placing the GPS antenna onto the top of specially-designed tubes, they measured the surface vertical positions in the summers of 2001 and 2002 at two sites in the Kuparuk River basin, Alaska. They reported a surface uplift of up to 6.7 cm between July 2001 and June 2002, and a subsequent subsidence of up to 2 cm between June and August 2002. The Circumpolar Active Layer Monitoring (CALM) program adopted the same protocol and conducted decade-long GPS campaigns at the end of thaw seasons in three continuous permafrost areas in northern Alaska (Shiklomanov et al., 2013; Streletskiy et al., 2016). However, these campaign GPS surveys have been only conducted annually.

In recent years, modern remote sensing methods have been utilized for mapping vertical displacements. Interferometric SAR (InSAR) has been used to quantify surface vertical deformation permafrost areas at seasonal and decadal timescales (Liu et al., 2010 and 2015). As a remote sensing method, InSAR is capable of measuring deformation over a large area (typically 100 km by 100 km). However, it still suffers from relatively long sampling intervals (about once per month) and loss of interferometric coherence for longer time series analysis. Moreover, InSAR measurements are fundamentally relative and need to be tied to a reference point, where the deformation is known or can be assumed to be zero. Over permafrost areas, it is not always conclusive about a stable reference point. Differential digital elevation models constructed from stereographic images or LiDAR have revealed surface elevation drops due to permafrost degradation (Lantuit and Pollard, 2005; Jones et al., 2013; Jones et al., 2015; Günther et al., 2015). However, these measurements typically only have annual or multi-year intervals, and the accuracy of elevation changes are on the order of sub-meters. Ground-based remote sensing tools, such as terrestrial laser scanning and ground-based InSAR, are emerging methods for measuring permafrost-related deformation within close ranges (Strozzi et al., 2014; Liu et al., 2016; Luo et al., 2017). However, most of these field surveys have been focusing on slope movements (for instance, rock glacier flow) and are campaign studies that only spanned a few days up to a few years.

In this study, we apply the GPS interferometric reflectometry (GPS-IR) technique (Larson, 2016) to the signal-to-noise ratio data collected by a continuous GPS receiver in Barrow, Alaska. This technique can retrieve the vertical distance between the antenna and surface reflector under the antenna. We will demonstrate that such a GPS-IR observable directly reflects the surface elevation changes due to dynamics of the frozen ground. We generate a time series of daily surface elevation changes on snow-free days over 12 summers. This new and unique dataset can quantify the seasonal, inter-annual, and decadal changes of the active layer and permafrost.

2. Key processes for surface vertical movement over flat terrains in continuous permafrost

In areas underlain by continuous permafrost, the surface vertical movement is largely related to the phase and volumetric change of ground ice. Here we briefly summarize the key processes for gradual surface vertical movement over flat terrains in continuous permafrost areas at annual, sub-decadal, to multi-decadal timescales.

5

At annual timescales, the active layer freezes and thaws. In the early freezing stage, water in the pore space freezes locally to pore ice. Such a phase change causes a ~9% volume expansion, resulting in surface uplift. However, such an uplift due to pore ice formation is not 'frost heave' as referred to by permafrost scientists. In cold continuous permafrost areas, two-directional freezing occurs within the active layer, i.e., from the surface downward and the permafrost table upward. Due to

10 the cryosuction processes, liquid water (soil moisture) migrates towards the freezing front near the base of the active layer, freezes and forms ice lens, termed as segregated (or segregational) ice (Smith, 1985; French, 2007). It is widely accepted that the ice segregation near the base of the active layer is responsible for annual surface heave. Reversely, in the following thaw season, pore and segregated ice within the active layer melts, volume decreases and thaw consolidation causes the ground to settle.

15

At sub-decadal to decadal timescales, vertical movements are controlled by ice conditions just beneath the active layer. Numerous permafrost studies suggest the existence of an ice-rich transition layer located between the base of the active layer and the top of the permafrost (Shur et al., 2005). In the literature, some call the top of the transition layer the 'transient layer', which can alter its status between seasonally thawing and freezing and perennially frozen at sub-decadal scales (e.g.,

20 Shur et al., 2005; French, 2007). We use 'transition layer' in this paper without further distinguishing the 'transient' layer from it. At the end of an exceptionally warm summer, the active layer deepens beyond its normal thickness and the ice-rich transition layer may thaw. As a result, enhanced surface subsidence would occur. In cold winters or cold summers, migrational water can form massive ice bodies within the transition layer, which becomes thicker and causes surface uplift.

25 If warming conditions persist for several decades or strong disturbances occur, the ice-rich transition layer would largely thaw, and permafrost degradation starts. Thaw subsidence due to permafrost degradation is gradual and homogenous at regional scales (Shiklomanov et al., 2013; Streletskiy et al., 2016). In areas where the near-surface permafrost is ice-rich, thermokarst processes would initiate at local scales upon thawing, causing abrupt and deep thaw as well as strong and irregular surface subsidence (Jorgenson 2008).

30 **3 Method**

3.1 GPS station SG27 and permafrost conditions

The continuous GPS station SG27 (156.610331W, 71.322895N) is in northern Barrow, next to the NOAA Barrow Observatory (Figure 1a). As part of the Plate Boundary Observatory (PBO) network, the main scientific objective of this station is to study solid earth movement, especially plate tectonics. The GPS receiver is attached to a wooden monument that is ~3.8 m above the ground surface (Figure 1b). The bottom of the monument is about 5 m beneath the surface. The station

5 has been operating and receiving L1 GPS signals since May 2002. It started receiving L2C signals in 2013. SG27 underwent two major instrumental changes, first on June 1 2004 and second on August 26 2010 (Table 1). The vertical shift in the GPS antenna phase center in 2010 was only 2 mm, having negligible effects in our data analysis and interpretation.

Table 1. History of equipment changes at SG27. The equipment codes follow the International GNSS Service convention
10 (ftp://igscb.jpl.nasa.gov/pub/station/general/rcvr_ant.tab).

Date	Receiver Change	Antenna Change (radome model code in parenthesis)
2004 June 1	TRIMBLE 4700 to TRIMBLE NETRS	TRM33429.20+GP (NONE) to TRM29659.00 (SCIS)
2010 August 26	N/A	TRM29659.00 (SCIS) to TRM59800.80 (SCIS)

The broad Barrow area is a flat coastal plain underlain by continuous permafrost. The upper part of the permafrost is ice-rich, with an ice content up to 75% in the top 2 m (Brown and Sellmann, 1973). Characterized by Arctic maritime climate, the summer is cool and moist. The thaw season in each year lasts from early June to late August. Within 90 m from SG27
15 (the footprint of the reflected GPS signals, see Section 2.2), the ground surface is flat, homogenous, polygon-free upland, and unaffected by thermokarst processes (Figure 1). The vegetation is mostly moist acidic tundra, typical for this region. The active layer is dominantly organic-rich soil that is nearly saturated during the thaw seasons. Active layer thickness (ALT) in 2016 was 53 cm with a standard deviation of 6 cm, obtained from mechanic probing at six locations within 90 m of SG27 (I. Go, personal communication, August 23 2016). Since the early 1990s, the CALM program has been measuring ALT every
20 mid-August at two sites, ~2 km southeast of SG27. They reported a mean ALT of 36 cm between 2004–2015 and no significant trend in the past 20 years (Shiklomanov et al., 2010 and updated data from https://www2.gwu.edu/~calm/data/north.html).

Streletskiy et al. (2016) conducted GPS campaigns and measured surface elevation in late August from 2003 to 2015 at four
25 plots in the ice-wedge dominated Cold Regions Research and Engineering Laboratory (CRREL) grid (~2 km southeast of SG27). Their measurements revealed that all these four plots subsided, at rates of 0.4 to 1 cm/year (2003–2015). Using a

stable benchmark to tie the surface elevation measured in 1962 to the same elevation reference frame of their GPS measurements, Streletskiy et al. (2016) found no net subsidence in the region over 41 years (1962–2003).
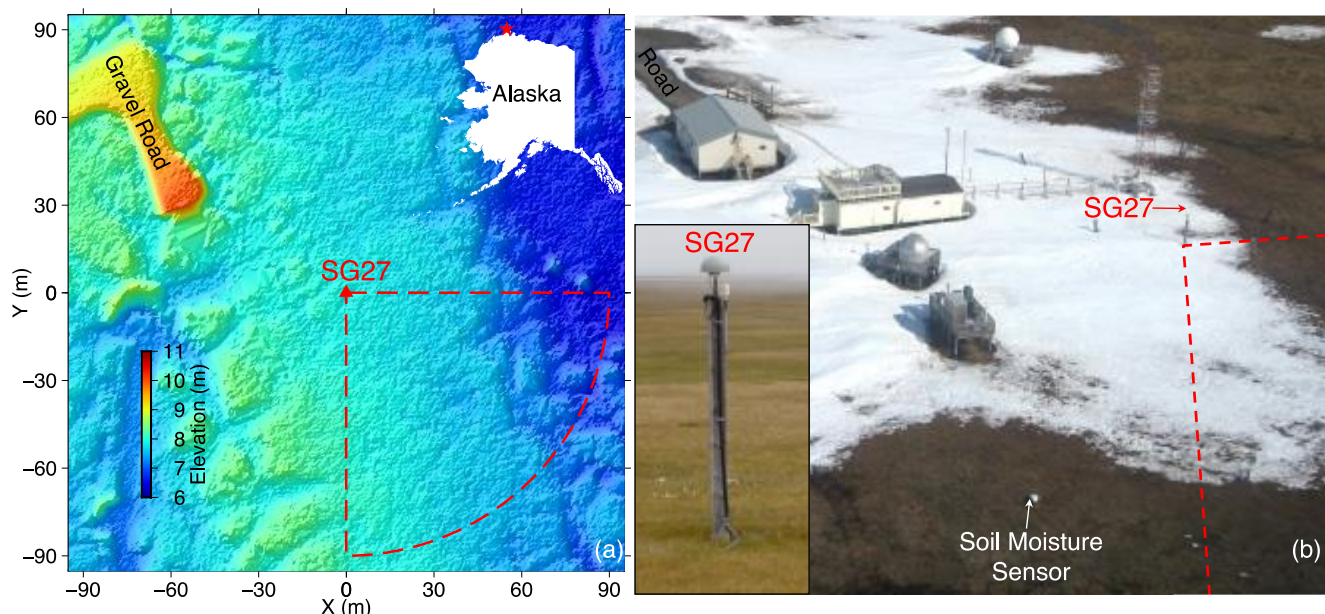
Figure 1. (a) Relief map of the area surrounding the GPS station SG27, produced using a LiDAR dataset collected in August 2012 (Wilson et al., 2014). The X and Y axes show horizontal and vertical positions relative to SG27 in UTM Zone 4N. The red dashed fan outlines the estimated footprint of the GPS reflected signals. The inset shows the location of Barrow as a red star in the northernmost of Alaska. (b) Aerial photograph over the facilities of the NOAA Barrow Observatory and SG27 (Photo: NOAA). The red dashed lines denote the western portion of the footprint. The inset is a close-up photograph of SG27, viewing from North (Photo: E. Jafarov, August 2013).

3.2 GPS Interferometric Reflectometry (GPS-IR)

GPS-IR is a technique that uses the interference between the direct and reflected GPS signals to infer ground reflector properties such as snow depth, soil moisture, and vegetation water content (Larson et al., 2008; Larson et al., 2009, Small et al., 2010). Larson (2016) provides an overview of the GPS-IR technique. Here we only describe the method of using GPS-IR to measure the reflector height, which refers to the height of the GPS receiver antenna's phase center above the reflecting surface.
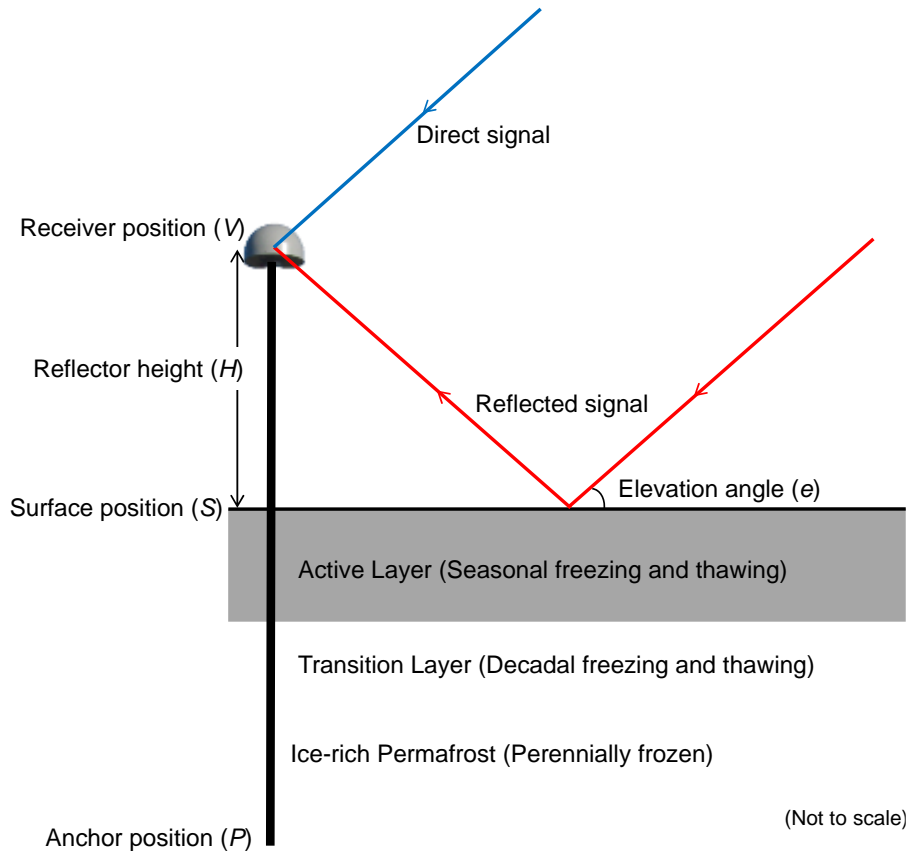
The Cryosphere
Open Access
Discussions
EGU

Figure 2. Schematic diagram of the GPS-IR geometry. The sub-surface in Barrow is depicted by a simplified three-layer model that consists of the active layer (~53 cm thick), the transition layer (thickness unknown), and the permafrost layer (>300 m thick). The top of permafrost is ice-rich.

5

GPS-IR uses the interference between the direct signal and the reflected signal from the ground surface. Figure 2 illustrates the interference geometry. The strength of the interference, quantified by the signal-to-noise ratio (SNR) of the received power, oscillates with the elevation angle (e). For a horizontal planar reflector, such as the flat surface surrounding SG27, the SNR oscillation is characterized by a dependency on sine of the elevation angle (Larson, 2016):

10 $$\text{SNR} = A \sin\left(\frac{4\pi H}{\lambda} \sin e + \phi\right), \qquad (1)$$

where A is the amplitude; H is the reflector height; λ is the wavelength of the GPS signal; and ϕ is the phase offset of the oscillation. Given a measure of varying SNR with $\sin e$, we calculate its periodogram using the Lomb-Scargle spectral analysis, determine the dominant frequency f, and eventually obtain the reflector height H as $f\lambda/2$. The reflection observed in SNR data using a geodetic antenna is most sensitive to the interface between air and the top soil layer.

15

We apply this method to the L1 SNR data (λ = 0.19029 m) recorded by SG27 to retrieve the reflector height at daily intervals. Using the SNR data from individual satellite track with an elevation angle range of 5 to 20 degrees, we estimate the reflector height and repeated for all tracks. To avoid the obstructions from buildings and other infrastructures located nearby (Figure 1b), we only keep the H with azimuth angles of 90 to 180 degrees (i.e., in the southeast quadrant). Then we average H from all usable tracks and use the average to represent the reflector height within the GPS-IR footprint. We calculate the standard error of the mean as the uncertainty of the averaged H. In fact, each track has a different reflecting point, which depends on the azimuth and elevation angles, as well as the antenna height. Using the first Fresnel zone of the reflected signals for the elevation angle of 5 degrees (Larson and Nievinski, 2013), we estimate the extent of the footprints as having a radius of 90 m from SG27 (Figure 1). To avoid the ambiguous interpretation about reflector height changes as caused by snow depth changes or by the thawing/freezing of soil, we only consider reflector height on snow-free days between July 1 and August 31 in each summer from 2004 to 2015. We exclude the data before 2004 to avoid a significant offset due to the GPS equipment change on June 1 2004.

3.3 Surface elevation changes in a geocentric frame and contribution from solid earth movement

For measuring surface elevation and its changes, an important issue is the reference frame. Leveling and GPS positioning measurements always adopt a geodetic datum. For instance, the surface positions from the campaign GPS studies of Streletskiy et al. (2016) in Barrow are in the North American Datum of 1983 (NAD83), an Earth-centered ('geocentric') ellipsoidal system.

By combining the daily reflector height and the vertical position of the GPS receiver, we can calculate the change of ground surface elevation at SG27 in a geocentric frame. Let V be the vertical position of the GPS receiver, then the vertical position of the ground reflector S is simply V minus H (Figure 2). We use the daily vertical positions of SG27 in the North America Fixed Reference Frame (NA12) from the GPS geodetic solutions published by the Nevada Geodetic Laboratory at the University of Nevada (http://geodesy.unr.edu/NGLStationPages/stations/SG27.sta). NA12 is aligned in origin and scale with the International Global Navigation Satellite Systems Service 2008 (IGS08) frame, and the vertical position in this frame is relative to the Earth-system center of mass (Blewitt et al., 2013).

It is worth reiterating that in a geocentric frame, the surface elevation changes (from either our GPS-IR or the GPS campaigns) are the summation from two independent processes: one is due to the dynamics of the active layer and near-surface permafrost (referred to as "frozen ground dynamics"), another is the movement of solid earth. Figure 2 illustrates how SG27, which was originally designed and set up as a PBO station, is used to study solid earth dynamics. Assuming the anchor position (P) is stable as it is deeply frozen in permafrost (at ~5 m depth) and the wooden pole is rigid, any change of the receiver's vertical position (V) is due to the movement of the solid earth. Figure 3 shows the time series of V in the

geocentric NA12 frame. The solid earth underwent regular cyclic vertical movements at the annual and semi-annual periods, due to surface mass loading (from the atmosphere, ocean, and surface hydrology), and a steady subsidence trend. The mean seasonal subsidence from July 1 to August 31 during 2004–2015 was 3.3 ± 0.2 cm. The best-fit linear subsidence trend was 0.27 cm/year.
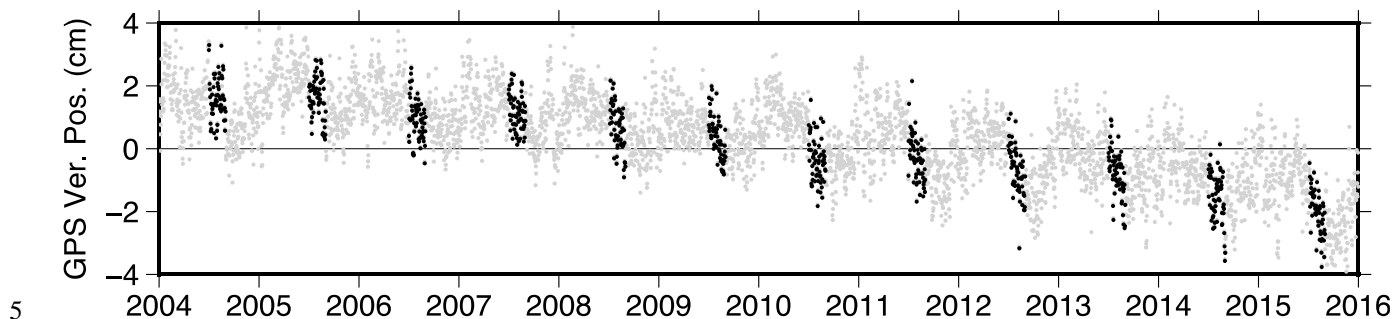

5   **Figure 3.** Time series of daily vertical positions of GPS receiver SG27 in the NA12 reference frame (source: http://geodesy.unr.edu/NGLStationPages/stations/SG27.sta). The mean has been removed. The black dots are from July 1 to August 31. The rest are shown as gray dots. To simplify the figure, uncertainties of the receiver positions are not shown.

10   As we have illustrated above, $S = V - H$ in a geocentric frame, therefore including the solid earth movement. This solid earth component needs to be removed for studying frozen ground dynamics. After this correction (i.e., subtracting by V), the surface elevation change due to frozen ground dynamics, denoted as S_F as a function of time t, is reduced to a simple negative relation with the reflector height:

$$S_F(t) = -H(t). \quad (2)$$

15   Therefore, the GPS-IR framework introduces an intrinsic convenience: we only need the reflector height H, rather than the GPS positioning solution V, for studying frozen ground dynamics. If not explicitly stated, all surface elevation results presented and discussed in the remainder of this paper are this $S_F(t)$ term in the geocentric NA12 frame. To directly compare S_F we estimate using GPS-IR and those obtained by the GPS campaigns of Streletskiy et al. (2016), we first convert their vertical position values from NAD83 to NA12, then remove V measured at SG27 from theirs. The solid-earth movement is

20   nearly the same at SG27 and the sites of Streletskiy et al. (2016), within 2 km distance in a tectonically inactive area.

3.4 Modeling seasonal subsidence due to the melting of pore ice in the active layer

We also model seasonal ground surface subsidence due to the melting of pore ice in the active layer in a forward manner and further assess the subsidence from the melting of segregated ice. For simplicity, the following conceptual and mathematical framework is for a given thaw season. Our forward model only considers one component in the seasonal subsidence that is

25   caused by the volume decrease from ice to water in the pores of the active layer as it thaws. Another component is the subsidence caused by thawing of segregated ice. We denote these two subsidence components as d_{pore} and d_{seg}, respectively.

The total thaw subsidence d is the sum of these two, i.e., $d = d_{\text{pore}} + d_{\text{seg}}$. We note that d is directly comparable to S_{F}. Throughout this paper, we use capitalized and lower-case symbols for the observed and modeled variables associated with vertical movement, respectively, and a hat accent (e.g., $\hat{S}_{\text{F}}$ in section 3.5) for the best-fit variables. Both d_{pore} and d_{seg} reach their seasonal maxima (denoted as $d_{\text{pore}}^{\max}$ and $d_{\text{seg}}^{\max}$, respectively) at the end of each thaw season. Because we know little

5   about massive cryogenic structures within the active layer near SG27, let alone their temporal changes, we cannot quantify d_{seg}. Instead, we model d_{pore} and interpret the difference between the observed or best-fit seasonal subsidence and d_{pore} as the contribution from melted segregated ice throughout a thaw season.

For a fully-saturated active layer, $d_{\text{pore}}^{\max}$ can be expressed as an integral over the entire active layer soil column (*Liu et al.*,

10   2014):

$$d_{\text{pore}}^{\max} = \int_0^L \phi(z) \frac{\rho_{\text{w}} - \rho_{\text{i}}}{\rho_{\text{i}}} dz, \qquad (4)$$

where z is the depth; dz is the incremental thickness of the thawed active layer soil column; ϕ is the soil porosity; ρ_{w} is the density of water; ρ_{i} is the density of pore ice; and L is ALT, which typically varies in different years. The mean ALT within the CALM grids was 39 cm in 2016. Assuming a constant ratio between the ALTs at SG27 and CALM (i.e., 53 cm/39 cm)

15   in the past years, we extrapolate the ALT at SG27 for 2004–2015 by multiplying the CALM ALT by this ratio. We follow Liu et al. (2012) and assume a surface organic layer with organic content decreasing exponentially with depth. We also estimate the uncertainties of the maximum thaw settlement by propagating the standard deviation of ALT measured within the footprint and the uncertainties in the assumed model parameters for calculating water content (Liu et al., 2012).

20   Next, we model cumulative subsidence due to top-down thawing of pore-ice on any day t since the thaw onset (T_{thaw}, late May to early June) until the freeze onset (T_{freeze}, late August to early September) as

$$d_{\text{pore}}(t) = \sqrt{\frac{DDT(t)}{DDT^{\max}}} d_{\text{pore}}^{\max} \qquad \text{if } T_{\text{thaw}} \le t \le T_{\text{freeze}}, \qquad (5)$$

where DDT is the degree day of thawing, monotonically increasing through the thaw season; $DDT^{\max}$ is the maximum DDT, corresponding to the end of the thaw season. The square root relationship derives from the Stefan equation that describes the

25   progressive downward migration of the thawing front (French, 2007; Liu et al., 2012). We calculate DDT using the daily-averaged 2-m air temperatures measured at the nearby NOAA Barrow Observatory.

3.5 Fitting observed seasonal subsidence using Stefan function

Considering both the GPS-IR measurement uncertainties and that some random processes other than the gradual downward

30   thawing may introduce random errors into our observed S_{F}, we fit the time series of S_{F} for each summer using the Stefan function in the same form as equation (5). The best-fit time series, denoted as $\hat{S}_{\text{F}}(t)$, differs from $S_{\text{F}}(t)$ by a random error term $\varepsilon(t)$, i.e.,

$$S_{\mathrm{F}}(t) = \hat{S}_{\mathrm{F}}(t) + \varepsilon(t) = \sqrt{\frac{DDT(t)}{DDT^{\max}}}\, \hat{S}^{\max} + \varepsilon(t), \qquad (6)$$

where $\hat{S}^{\max}$ is the maximum accumulative subsidence within each thaw season. This $\hat{S}^{\max}$ term is the only coefficient that we fit using the least squares inversion.

5 Since the DDT records spanned from the thaw onset till the freezing onset, we can also use equation (6) to extrapolate our observed S_{F} that spanned July 1 to August 31 back to the thaw onset, around June 1. Because surface subsidence is fast in early thaw season and gradually slows down toward the end of the thaw, this extrapolation is important if one needs to consider the net change during the entire thaw season.

4 Results

10 ### 4.1 Time series of daily surface elevation changes

Figure 4a shows the time series of surface elevation changes due to frozen ground dynamics from 2004 to 2015. We only present the values of S_{F} on snow-free days between July 1 and August 31 and exclude a few unreliable estimates. The ground surface underwent gradual seasonal subsidence. Figure 4a also shows prominent inter-annual variability, which is associated with summer air temperatures. Using the DDT at the end of each thaw season as an indicator of warm/cool

15 summers (Figure 4b), we observe larger seasonal subsidence within warm thaw seasons such as 2004 and 2007 and smaller seasonal subsidence within cool summers such as 2005, 2006, and 2014. At secular scales, the ground surface underwent a steady subsidence of 1.05 ± 0.03 cm/year from 2004 to 2010, followed by an uplift trend of 1.82 ± 0.06 cm/year from 2011 to 2014, and then a subsidence from 2014 to 2015. The overall subsidence trend between 2004 and 2015 was 0.26 ± 0.02 cm/year.
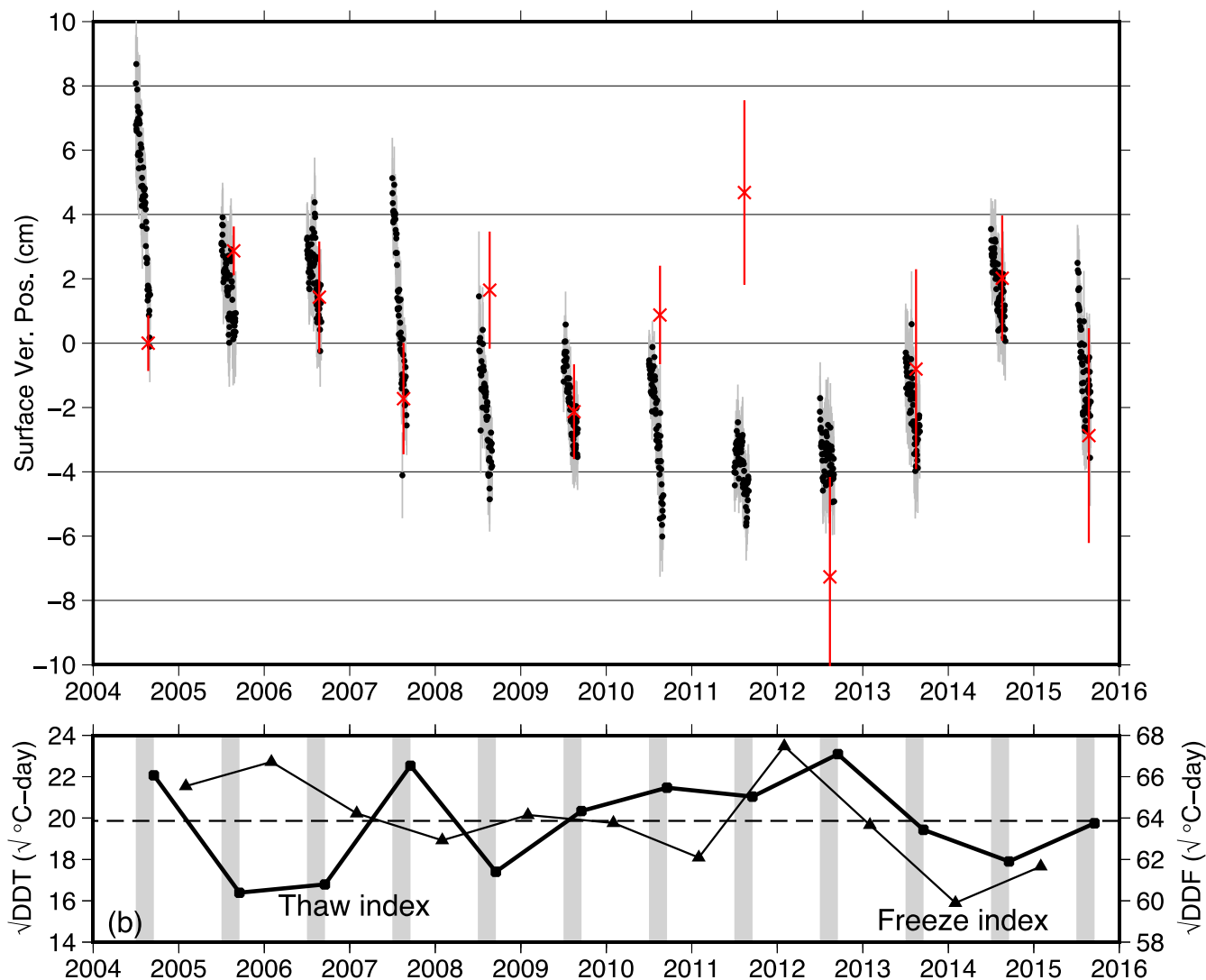
20

Figure 4. (a) Demeaned time series of surface vertical position. The black dots are the daily vertical positions of the surface reflector at SG27, retrieved using GPS-IR. The error bars (standard error of the mean) are shown in gray. The red crosses are the vertical positions of ground measured annually in mid-August by Streletskiy et al. (2016), averaged over four plots at the CRREL grid, solid earth movement removed (see section 2.3). The red error bars show the standard deviation of the four plots. (b) Time series of the square root of degree day of thawing (DDT) at the end of each thaw season (squares, labeled as 'Thaw index') and the square root of degree day of freezing (DDF) at the end of each frozen season (triangles, labeled as 'Freeze index', and manually shifted to the mid of each frozen season for visual clarity). The dotted line is the 2004–2015 mean level, overlapping for both indices. The gray bars denote July 1 to August 31 in each year.

4.2 Comparison between the GPS-IR and in situ GPS campaign measurements

11

Our estimated surface elevation changes agree well with the in situ measurements made by Streletskiy et al. (2016) in an area dominated by ice wedges (~2 km southeast of SG27). Since the in situ measurements were conducted in late August, we can only compare these two in the inter-annual sense (Figure 3a). Both sets of elevation change results are consistent within the uncertainties in individual years except 2008, 2010, 2011, and 2012. Both show similar subsidence trends between 2004

5   and 2010, and similar uplift trends during 2012–2014, and the subsidence from 2014 to 2015. The overall subsidence trend of the in situ measurements was 0.19 ± 0.14 cm/year between 2004 and 2015, which is consistent with the overall trend of ours (i.e., 0.26 ± 0.02 cm/year) within the estimated uncertainties. The in situ trend is smaller than the reported values in Streletskiy et al. (2016) because we have removed V, which has a linear subsidence trend of 0.27 cm/year, from their GPS measurements (see Section 3.3).

10

Out of the four mismatched years, the in situ measurements show strong heave from the previous August in three of them (i.e., heave from 2007 to 2008, from 2009 to 2010, from 2010 to 2011). Streletskiy et al. (2016) did not explicitly explain these observed heaves. We cannot explain them by strong ground uplift during winters as none of these three winters were particularly cold (their freeze indices were at the mean level, Figure 3c) or during cool summers (the thaw indices of 2009

15   and 2011 were higher than the mean level, Figure 3c). The in situ measurements also show ~13 cm of subsidence from August 2011 to August 2012, in contrast to the nearly zero changes between these two Augusts from our GPS-IR based observations.

4.3 Comparison among the observed, best-fit, and modeled seasonal subsidence

20   Figure 5 shows the year-by-year comparison between the GPS-IR results and the best-fit model. This simple model fits the observed elevation changes well, with R^2 values ranging from 0.24–0.9 and a mean of 0.6 for all the years. The fitting is poor for those years when the dynamic range of S_F was small, for instance, in 2011 and 2012.

The second column of Table 2 lists the elevation drops between each July 1 and August 31, obtained from the best-fit results

25   (i.e., the solid cyan line in Figure 5). From year to year, this net subsidence ranged from 1.1 to 7.4 cm, with a 12-year mean of 3.4 cm and a standard deviation of 2.1 cm. Extending the best-fit results to June 1 (the dashed cyan lines in Figure 5), we infer that the total subsidence within each thaw season ranged from 1.8 to 12.5 cm, with a 12-year mean of 5.8 cm and a standard deviation of 3.5 cm (Table 2, third column). The uncertainties of these best-fit values (second and third columns of Table 2) are estimated using the weighted least squares optimization. Our modeled subsidence due to the melting of pore ice

30   spanning each thaw season was 2.8 cm on average, with a small inter-annual variability (Table 2, fourth column). This modeled mean is smaller than the best-fit mean by 3.0 cm. The uncertainties of the modeled values are estimated using the method described in Liu et al. (2012). The residual between the extended best-fit and the modeled pore ice contribution is our estimated seasonal subsidence due to the melting of segregated ice (i.e., d_{seg}^{max}, listed in the last column of Table 2). The

uncertainties of $d_{\text{seg}}^{\text{max}}$ are obtained by error propagation. In 8 out of 12 years, our inferred $d_{\text{seg}}^{\text{max}}$ are larger than the uncertainties, which will be used in the following analysis.
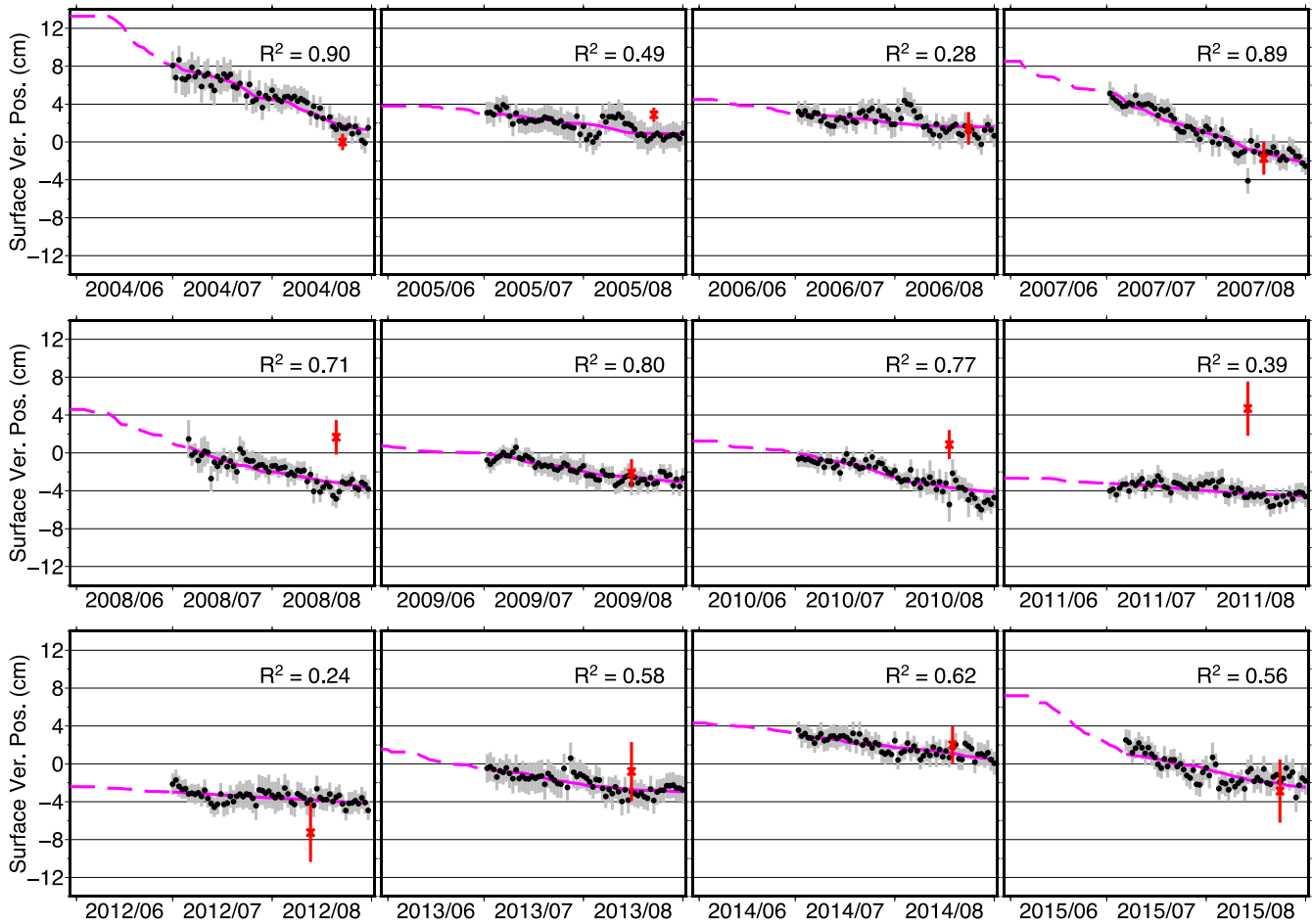

Figure 5. Similar to Figure 4a, but shows the time series in each year from 2004 to 2015. Adding from Figure 4a are the solid cyan lines, which are the best-fit seasonal changes of surface elevation using equation (6). The R^2 value of the fit is labeled on each figure. The dashed cyan lines denote the extended records back to June 1 (see Section 3.3).

Since the subsidence caused by melting of segregated ice (i.e., $d_{\text{seg}}^{\text{max}}$) is controlled by the total amount of segregated ice in the active layer before thawing, we hypothesize that more segregated ice may develop during a cold winter, therefore resulting in a larger subsidence during the following thaw season. We further test this relationship using a scatter plot between $d_{\text{seg}}^{\text{max}}$ and the square-root of DDF for the previous freeze season (Figure 6). Although we observe an overall increasing trend,

13

the linear relationship is statically insignificant ($R^2 = 0.24$). This poor fitting is mostly because of three 'outliers', i.e., 2009, 2010, and 2013. If we exclude these from the regression, the R^2 value increases to 0.88.

Table 2. Comparison among the best-fit subsidence between July 1 and August 31, extended best-fit subsidence between June 1 and August 31 (i.e., entire thaw season), and the modeled maximum subsidence due to the melting of pore ice in the active layer. The last column is the difference between the extended best-fit and the modeled maximum subsidence, regarded as the net subsidence due to the melting of segregated ice. In the last column, the estimated subsidence values larger than the uncertainties are highlighted in bold.

|	Net seasonal subsidence (cm)			
Year	Best-fit (July 1 to August 31)	Extended Best-fit (June 1 to August 31)	Modeled due to melting of pore ice	Estimated due to melting of segregated ice
2004	7.0 ± 0.3	12.5 ± 0.5	3.1 ± 1.1	**9.4 ± 1.6**
2005	2.1 ± 0.3	2.9 ± 0.3	2.6 ± 0.9	0.3 ± 1.4
2006	1.3 ± 0.3	3.1 ± 0.6	2.5 ± 0.9	0.6 ± 1.5
2007	7.4 ± 0.3	10.6 ± 0.4	2.5 ± 0.9	**8.1 ± 1.4**
2008	4.3 ± 0.4	8.5 ± 0.7	2.6 ± 0.8	**5.8 ± 1.5**
2009	2.9 ± 0.2	4.4 ± 0.3	2.6 ± 0.9	**1.8 ± 1.4**
2010	4.1 ± 0.3	5.3 ± 0.4	3.0 ± 0.8	**2.3 ± 1.4**
2011	1.3 ± 0.2	2.0 ± 0.3	3.0 ± 1.0	-1.0 ± 1.5
2012	1.1 ± 0.2	1.8 ± 0.4	2.8 ± 0.8	-1.0 ± 1.3
2013	2.4 ± 0.3	4.8 ± 0.5	3.0 ± 1.1	**1.8 ± 1.5**
2014	2.6 ± 0.3	4.4 ± 0.4	2.7 ± 0.8	**1.7 ± 1.3**
2015	3.5 ± 0.2	9.1 ± 1.0	2.9 ± 0.8	**6.1 ± 1.6**
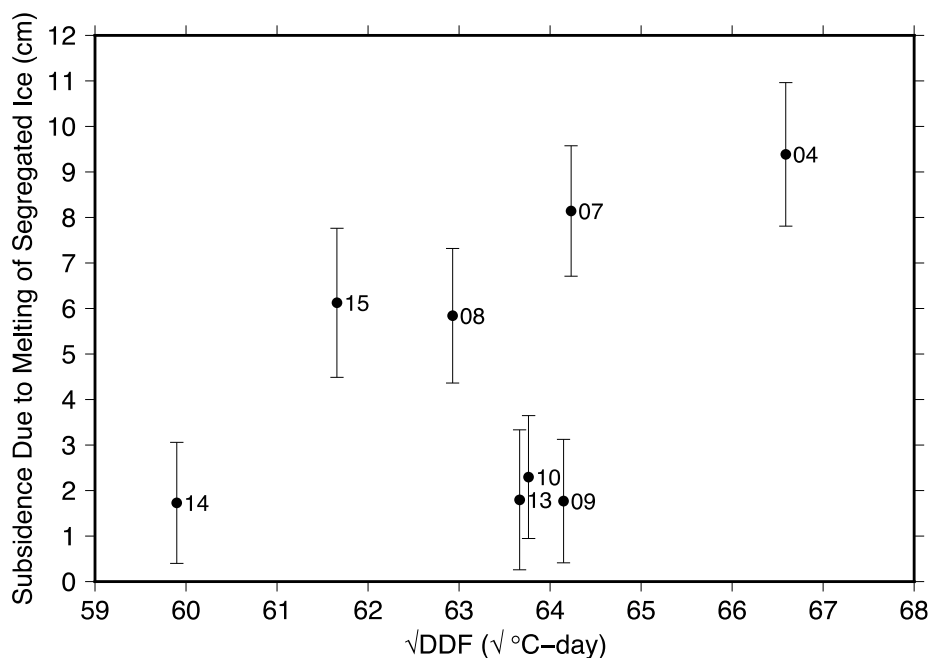
Figure 6. Scatter plot between the estimated subsidence due to the melting of segregated ice in the active layer and the square root of DDF of the previous freeze season. The labels refer to the years of the thaw seasons.

5. Discussion

5.1 Thawing/freezing of the transition layer as a mechanism for sub-decadal subsidence/uplift

We postulate that both large excess seasonal subsidence and the decadal subsidence trend are due to thawing of the transition layer in warm summers. Figure 4a shows that the largest seasonal surface subsidence occurred in 2004 and 2007, which were the warmest summers during the 12 years (Figure 4b). The thaw indices also increased gradually from 2005 to 2013, which may cause the gradual thawing of the transition layer and thus the linear surface subsidence trend during the same period. Conversely, after a cooler summer or in a colder winter, significant accretions of segregated ice can develop within the transition layer and cause surface heave during the freezing period. This mechanism can also explain the transient uplift trend between 2012 and 2015, during which the thaw indices and freeze indices were lower than normal.

The transition layer is widely thought to act as a buffer between the thawing of the active layer and ice-rich permafrost in that it protects the permafrost beneath from thawing. The progressive thawing of the transition layer causes a gradual surface subsidence that is hardly observable without accurate measurements over decades. In addition to the campaign GPS studies conducted by Shiklomanov et al. (2013) and Streletskiy et al. (2016), as well as the InSAR study of Liu et al. (2010), our GPR-IR-based results provide another set of observations of such subtle decadal changes on the North Slope of Alaska.

5.2 Effects of soil moisture on the retrieved reflector height

Soil moisture greatly affects the dielectric constant of the ground reflector and thus the multipath modulation (Nievinski and Larson, 2014a). Temporal changes of soil moisture can cause apparent changes in the retrieved reflector heights. As this apparent change is due to surface compositional properties, we follow Nievinski (2013) to refer to this as the 'compositional height'. We need to assess the compositional heights due to soil moisture changes.

We first estimate the general varying pattern of the compositional height with changing soil moisture (in volumetric water contents, VWC) that increase from 0 to 1 by an interval of 0.01. For organic-rich soils with a given VWC, we run the GPS multipath simulator of Nievinski and Larson (2014b), named "MPSImulator" (publicly available at https://www.ngs.noaa.gov/gps-toolbox/MPsimul.htm), to simulate SNR data using the same settings as the real SNR data at SG27 (see Table 3 for a list of simulator settings). Then we apply the same GPS-IR method as described in section 2.2 to calculate the reflector height. Because of the changes of antenna and radome on August 24 2010, we run the simulator using two antenna models and obtain two relationships of apparent reflector heights versus soil moisture. Because the simulator does not include gain pattern models of the two antenna-radome combinations at SG27, we set the radome models as 'SCIS' and 'NONE' for the two cases, respectively. The changes of compositional height from its lowest value are shown in Figure 7. Both curves show increasing reflector height with soil moisture. In the post-2010 case, the reflector height shows a higher sensitivity to soil moisture than the pre-2010 case.

Table 3. Key settings used in MPSImulator. The others are set to the defaults.

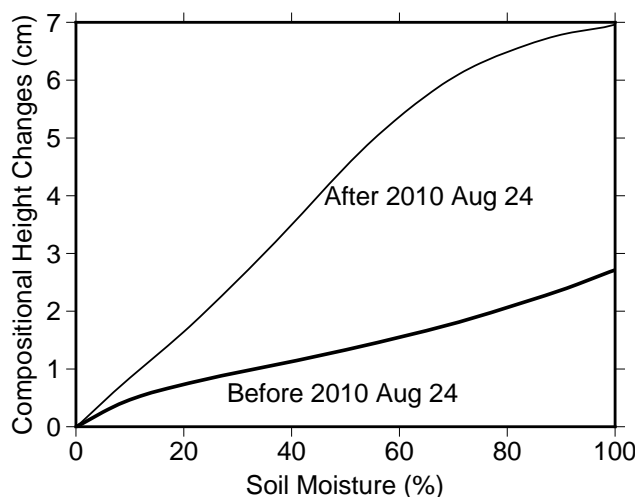| Frequency Name	L1
Code Name	C/A
Elevation Angles	5–20 degrees
Azimuth Angles	90–180 degrees
Antenna Height	3.8 m
Medium Materials	Loam; volumetric soil moisture varying from 0 to 100%
Antenna Model	TRM29659.00 before 2010/08/24
	TRM59800.80 after 2010/08/24
Radome Model	SCIS before 2010/08/24
	NONE after 2010/08/24

Figure 7. Changes of compositional height (i.e. apparent reflector height) with soil moisture (volumetric water content) based on the simulated SNR data using two antenna models: TRM29659.00 was used "Before 2010 Aug 24"; TRM59800.80 was used "After 2010 Aug 24".

5

Next, we consider a more realistic case by using soil moisture data obtained near SG27 during July and August. Specifically, we use the volumetric water content measured nearly daily at the Barrow CALM soil-climate site "U1-1", located approximately 60 m south-southeast of SG27 (Figure 1b). The period of the publicly-available dataset is from late August in 1995 to the end of 2011. Figure 8a shows the time series of VWC at 5 cm depth, starting from 1996. Five cm is the resolved

10 depth range for soil moisture retrievals using GPS-IR (Larson et al., 2008). Within each July and August, the soil moisture typically varied within 10–15%, with 2009 showing the largest range of ~25%. In many summers, the soil moisture first decreased from June to July, then increased in August. Rainfall events sharply increased the soil moisture (e.g., in 2010 and 2011).
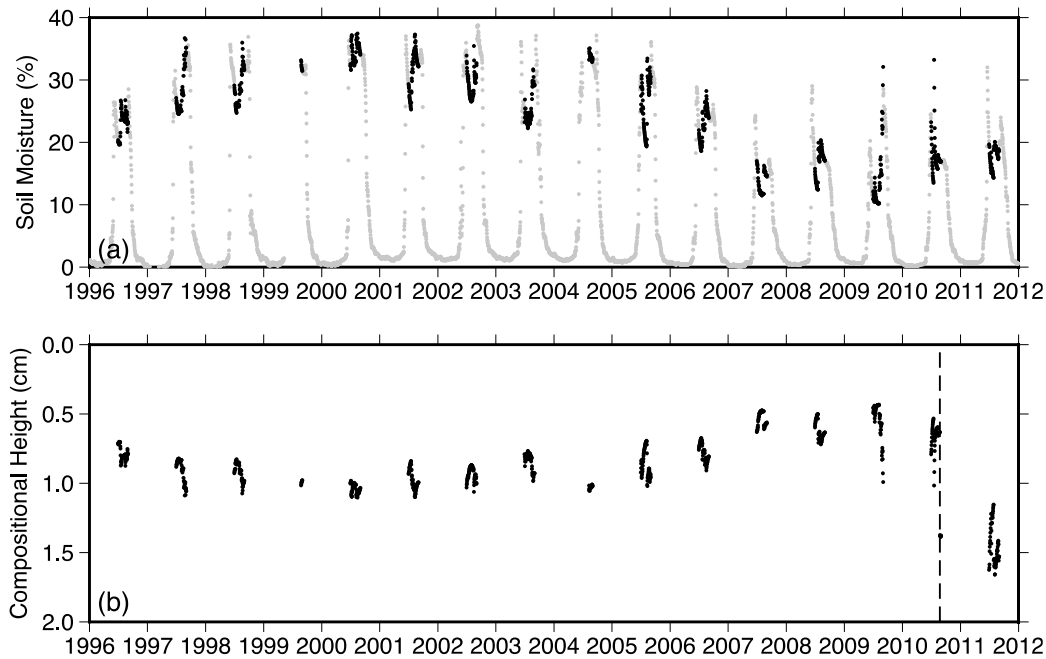
Figure 8. (a) Daily soil moisture at 5 cm depth, measured at CALM Barrow soil-climate site 'U1-1'. Black dots and gray dots denote records during July-August and in other months, respectively. The records have data gaps in the summers of 2000 and 2004. (b) The simulated changes of reflector height in July and August. The vertical dashed line denotes the date of antenna change (August 24 2010).

Using the modeled relationship as shown in Figure 7 and the soil moisture records (Figure 8a), we then simulate the changes of compositional height (Figure 8b). Because the soil moisture records are not from within the GPS-IR footprint and their period does not fully overlap with our GPS-IR records, we cannot use the simulated compositional heights to 'correct' the GPS-IR reflector height results. Instead, we interpret the simulated results to assess the possible effects of soil moisture, in the following aspects. First, in our case using the settings listed in Table 3, the compositional heights are always positive. However, because we are only interested in temporal changes, any systematic bias due to soil moisture changes is irrelevant. Second, the changes of compositional height within each summer were within in 0.5 cm, much smaller than the reflector height changes at seasonal scales. Third, the largest inter-annual change in compositional height was between 2010 and 2011, due to the antenna change. For instance, the compositional height increased by ~0.8 cm between July 1 2010 and July 1 2011. This is still smaller than the ~3.2 cm subsidence based on the GPS-IR reflector height records. Fourth, because the near-surface soil moisture in Barrow did not undergo any significant decadal changes, the secular trend of compositional height was negligible (e.g., 6.4×10^{-5} cm/year for 1996–2010 and 1.4×10^{-5} cm/year for 1996–2011). Given the above reasons, we conclude that our GPS-IR-retrieved changes of ground surface elevation are not significantly affected by these soil moisture effects.

5.3 Merits and limitations of long-lasting, daily GPS-IR measurements for frozen ground studies

The surface elevation changes retrieved from our GPS-IR measurements are daily and long-lasting, which are unique and valuable for quantifying subtle surface changes over permafrost areas. In cases of no major instrumental changes or that any vertical shift in GPS antenna phase center due to instrument change is known (e.g., 2 mm in 2010 for SG27), the GPS-IR-

5   based measurements are consistent, sustained, and progressively increasing. This is important for studying seasonal, inter-annual, and long-term dynamics of the active layer and permafrost. In situ ALT or GPS measurements have been conducted annually, but not always on the same day of the year due to logistical constraints. Because the seasonal changes are more significant than the inter-annual and long-term changes, the latter two estimated from a poorly sampled record may be aliased by the seasonal changes (Liu et al., 2015). Our records can avoid such aliasing problem.

10

Since the GPS-IR-estimated reflector height directly reflects the frozen ground dynamics, it is convenient for permafrost scientists who do not need to process geodetic-level GPS positioning data or correcting for the solid earth movement. Knowing the GPS receiver position, nonetheless, we can obtain the 'absolute' surface ground elevation changes in a geocentric frame (i.e., the S term). This type of geocentric records can be directly compared with altimetry observations and

15   be used to tie locally-reference measurements, such as InSAR. For instance, the surface elevation changes we have obtained at SG27 would serve as a good reference point to tie InSAR measurements to the geocentric earth frame. The daily records would also complement InSAR measurements by filling their temporal gaps.

However, GPS-IR suffers from a few limitations. Firstly, the day-to-day variations in our retrieved reflector height are

20   unreliable, due to relatively large uncertainties (cm level in the case of SG27) and the soil moisture effects. Therefore, we choose not to interpret the daily changes in our time series as associated with frozen ground dynamics. Second, GPS-IR signals on snow-covered days are dominated by snow depth changes, limiting the use of this type of data for studying ground surface changes on snow-free days. Nonetheless, as we have demonstrated in this study, noisy daily records continuously spanning over 60 days in each summer and over 12 years can provide robust estimates of seasonal, inter-annual, and decadal

25   changes. Third, similar to typical in-situ observations, GPS-IR only offers site-specific measurements. We note that the GPS-IR method takes spatial averages within the reflection footprint (~90 m radius in the case of SG27). This averaging helps to mitigate the spatial heterogeneities due to changes in soil and vegetation, as well as active layer and ground ice conditions. Lastly, reliable GPS-IR retrieval requires a smooth surface within the footprint. Therefore, this method is likely to fail over thermokarst landforms.

30

6 Conclusions

Using a continuously-running station mounted deep into permafrost in Barrow, we show that the reflector height retrieved

using GPS-IR can estimate surface elevation changes during thaw seasons at a daily interval. This 12-year-long record offers quantitative insights about the seasonal, inter-annual, and decadal variabilities of the flat terrain in continuous permafrost. Such continuous, consistent, daily records spanning over a long time are of great value to monitoring permafrost changes in a changing climate. The GPS-IR data can also help to fill in the temporal gaps in other field-based or remote sensing

5   methods, and tie relative measurements, such as InSAR, to the geocentric frame.

This method could be potentially extended to numerous continuous global navigation satellite system receivers operating in cold regions. Our study also highlights the importance of long-lasting measurements of active layer thickness, soil moisture, ground temperature, and surface elevation changes, ideally at the same location, for a comprehensive and quantitative

10   understanding of near-surface dynamics of the active layer and permafrost.

20   **References**

Blewitt, G., Kreemer, C., Hammond, W. C., and Goldfarb, J. M.: Terrestrial reference frame NA12 for crustal deformation studies in North America, Journal of Geodynamics, 72, 11–24, doi:10.1016/j.jog.2013.08.004, 2013.

Brown, J. and Sellmann, P. V.: Permafrost and coastal plain history of Arctic Alaska, in: Alaskan Arctic Tundra, edited by Britton, M. E., 25, pp. 31–47, 1973.

25   French, H. M.: The Periglacial Environment, John Wiley & Sons, Ltd, third edn., 2007.

Günther, F., Overduin, P. P., Yakshina, I. A., Opel, T., Baranskaya, A. V., and Grigoriev, M. N.: Observing Muostakh disappear: permafrost thaw subsidence and erosion of a ground-ice-rich island in response to arctic summer warming and sea ice reduction, The Cryosphere, 9, 151–178, doi:10.5194/tc-9-151-2015, 2015.

Jones, B. M., Stoker, J. M., Gibbs, A. E., Grosse, G., Romanovsky, V. E., Douglas, T. A., Kinsman, N. E. M., and

30   Richmond, B. M.: Quantifying landscape change in an Arctic coastal lowland using repeat airborne LiDAR, Environmental Research Letters, 8, 045025, doi:10.1088/1748-9326/8/4/045025, 2013.

Jones, B. M., Grosse, G., Arp, C. D., Miller, E., Liu, L., Hayes, D. J., and Larsen, C. F.: Recent Arctic tundra fire initiates widespread thermokarst development, Scientific Reports, 5, 15865, doi:10.1038/srep15865, 2015.

Lantuit, H. and Pollard, W. H.: Temporal stereophotogrammetric analysis of retrogressive thaw slumps on Herschel Island, Yukon Territory, Natural Hazards and Earth System Science, 5, 413–423, doi:10.5194/nhess-5-413-2005, 2005.

5   Larson, K. M.: GPS interferometric reflectometry: applications to surface soil moisture, snow depth, and vegetation water content in the western United States, Wiley Interdisciplinary Reviews: Water, 3, 775–787, doi:10.1002/wat2.1167, 2016.

Larson, K. M. and Nievinski, F. G.: GPS snow sensing: results from the EarthScope Plate Boundary Observatory, GPS Solutions, 17, 41–52, doi:10.1007/s10291-012-0259-7, 2013.

Larson, K. M., Small, E. E., Gutmann, E. D., Bilich, A. L., Braun, J. J., and Zavorotny, V. U.: Use of GPS receivers as a soil
10   moisture network for water cycle studies, Geophysical Research Letters, 35, L24405, doi:10.1029/2008GL036013, 2008.

Larson, K. M., Gutmann, E. D., Zavorotny, V. U., Braun, J. J., Williams, M. W., and Nievinski, F. G.: Can we measure snow depth with GPS receivers?, Geophysical Research Letters, 36, L17502, doi:10.1029/2009GL039430, 2009.

Little, J., Sandall, H., Walegur, M., and Nelson, F.: Application of Differential Global Positioning Systems to monitor frost heave and thaw settlement in tundra environments, Permafrost and Periglacial Processes, 14, 349–357, doi:10.1002/ppp.466,
15   2003.

Liu, L., Zhang, T., and Wahr, J.: InSAR measurements of surface deformation over permafrost on the North Slope of Alaska, Journal of Geophysical Research: Earth Surface, 115, F03023, doi:10.1029/2009JF001547, 2010.

Liu, L., Schaefer, K., Zhang, T., and Wahr, J.: Estimating 1992–2000 average active layer thickness on the Alaskan North Slope from remotely sensed surface subsidence, Journal of Geophysical Research: Earth Surface, 117, F01005,
20   doi:10.1029/2011JF002041, 2012.

Liu, L., Schaefer, K., Gusmeroli, A., Grosse, G., Jones, B. M., Zhang, T., Parsekian, A., and Zebker, H.: Seasonal thaw settlement at drained thermokarst lake basins, Arctic Alaska, The Cryosphere, 8, 815–826, doi:10.5194/tc-8-815-2014, 2014.

Liu, L., Jiang, L., Liu, L., Gao, B., Sun, Y., Wang, H., and Zhang, T.: First measurements of permafrost-related surface movements using ground based SAR interferometry: A case study in the Eboling Mountain on the Qinghai-Tibet Plateau, in:
25   XI. International Conference on Permafrost, edited by Günther, F. and Morgenstern, A., 2016.

Mackay, J. and Leslie, R.: A simple probe for the measurement of frost heave within frozen ground in a permafrost environment, Current research, part A. Geological Survey of Canada, pp. 37–41, 1987.

Mackay, J. R.: Downward water movement into frozen ground, western Arctic coast, Canada, Canadian Journal of Earth Sciences, 20, 120–134, doi:10.1139/e83-012, 1983.

30   Mackay, J. R. and Burn, C. R.: The first 20 years (1978-1979 to 1998-1999) of active-layer development, Illisarvik experimental drained lake site, western Arctic coast, Canada, Canadian Journal of Earth Sciences, 39, 1657–1674, 2002.

Nievinski, F. G.: Forward and inverse modeling of GPS multipath for snow monitoring, Ph.D. thesis, University of Colorado, 2013.

Nievinski, F. G. and Larson, K. M.: Forward modeling of GPS multipath for near-surface reflectometry and positioning applications, GPS Solutions, 18, 309–322, doi:10.1007/s10291-013-0331-y, 2014a.

Nievinski, F. G. and Larson, K. M.: An open source GPS multipath simulator in Matlab/Octave, GPS Solutions, 18, 473–481, doi:10.1007/s10291-014-0370-z, 2014b.

5 Schaefer, K., Liu, L., Parsekian, A., Jafarov, E., Chen, A., Zhang, T., Gusmeroli, A., Panda, S., Zebker, H. A., and Schaefer, T.: Remotely Sensed Active Layer Thickness (ReSALT) at Barrow, Alaska using Interferometric Synthetic Aperture Radar, Remote Sensing, 7, 3735–3759, doi:10.3390/rs70403735, 2015.

Shiklomanov, N. I., Streletskiy, D. A., Nelson, F. E., Hollister, R. D., Romanovsky, V. E., Tweedie, C. E., Bockheim, J. G., and Brown, J.: Decadal variations of active-layer thickness in moisture-controlled landscapes, Barrow, Alaska, Journal of
10 Geophysical Research: Biogeosciences, 115, G00I04, doi:10.1029/2009JG001248, 2010.

Shiklomanov, N. I., Streletskiy, D. A., Little, J. D., and Nelson, F. E.: Isotropic thaw subsidence in undisturbed permafrost landscapes, Geophysical Research Letters, 40, 6356–6361, doi:10.1002/2013GL058295, 2013.

Shur, Y., Hinkel, K. M., and Nelson, F. E.: The transient layer: implications for geocryology and climate-change science, Permafrost and Periglacial Processes, 16, 5–17, doi:10.1002/ppp.518, 2005.

15 Small, E. E., Larson, K. M., and Braun, J. J.: Sensing vegetation growth with reflected GPS signals, Geophysical Research Letters, 37, L12401, doi:10.1029/2010GL042951, 2010.

Smith, M.: Models of soil freezing, in: Field and theory: Lectures in geocryology, edited by Church, M. and Slaymaker, O., pp. 96–120, University of British Columbia Press, Vancouver, BC, 1985.

Streletskiy, D. A., Shiklomanov, N. I., Little, J. D., Nelson, F. E., Brown, J., Nyland, K. E., and Klene, A. E.: Thaw
20 subsidence in undisturbed tundra landscapes, Barrow, Alaska, 1962–2015, Permafrost and Periglacial Processes, doi:10.1002/ppp.1918, 2016.

Strozzi, T., Raetzo, H., Wegmüller, U., Papke, J., Caduff, R., Werner, C., and Wiesmann, A.: Satellite and terrestrial radar interferometry for the measurement of slope deformation, in: Engineering Geology for Society and Territory-Volume 5, pp. 161–165, Springer, 2015.

25 Wilson, C., Gangodagamage, C., and Rowland, J.: Digital Elevation Model, 0.5 m, Barrow Environmental Observatory, Alaska, 2012, in: Next Generation Ecosystem Experiments Arctic Data Collection, Carbon Dioxide Information Analysis Center, Oak Ridge National Laboratory, Oak Ridge, Tennessee, USA, doi:10.5440/1109234, 2014.